

Predicting Pulsar Scintillation from Refractive Plasma Sheets

Dana Simard,^{1,2,3*} Ue-Li Pen^{1,4,3,5}

¹Canadian Institute for Theoretical Astrophysics, University of Toronto, 60 Saint George Street, Toronto, ON M5S 3H8, Canada

²Department of Astronomy and Astrophysics, University of Toronto, 50 Saint George Street, Toronto, ON M5S 3H4, Canada

³Dunlap Institute for Astronomy and Astrophysics, University of Toronto, 50 Saint George Street, Toronto, ON M5S 3H4, Canada

⁴Canadian Institute for Advanced Research, Program in Cosmology and Gravitation, Toronto, ON M5G 1Z8, Canada

⁵Perimeter Institute for Theoretical Physics, 31 Caroline Street North, Waterloo, ON N2L 2Y5, Canada

Accepted XXX. Received YYY; in original form ZZZ

ABSTRACT

The dynamic and secondary spectra of many pulsars show evidence for long-lived, aligned images of the pulsar that are stationary on a thin scattering sheet. One explanation for this phenomenon considers the effects of wave crests along sheets in the ionized interstellar medium, such as those due to Alfvén waves propagating along current sheets. If these sheets are closely aligned to our line-of-sight to the pulsar, high bending angles arise at the wave crests and a selection effect causes alignment of images produced at different crests, similar to grazing reflection off of a lake. Using geometric optics, we develop a simple parameterized model of these corrugated sheets that can be constrained with a single observation and that makes observable predictions for variations in the scintillation of the pulsar over time and frequency. This model reveals qualitative differences between lensing from overdense and underdense corrugated sheets: Only if the sheet is overdense compared to the surrounding interstellar medium can the lensed images be brighter than the line-of-sight image to the pulsar, and the faint lensed images are closer to the pulsar at higher frequencies if the sheet is underdense, but at lower frequencies if the sheet is overdense.

Key words: pulsars: general – ISM: general – ISM: structure

1 INTRODUCTION

Observations of pulsar scintillation, the variation in intensity over frequency and time due to propagation effects induced by the interstellar medium (ISM), have revealed significant structure in the secondary spectrum (the 2-dimensional power spectrum of the dynamic spectrum, the intensity of the pulsar over time and frequency). In particular, a parabolic distribution of power in the secondary spectrum has been found to be common in pulsars imaged with sufficient dynamic range and resolution (Putney et al. 2005; Stinebring et al. 2001). In some pulsars, inverted arclets with apexes along the main parabolic arc are also present (Hill et al. 2005; Stinebring 2007); see Brisken et al. (2010, figure 1) for a particularly striking example. These parabolic arcs can arise if the scattering is highly anisotropic and localized at a thin scattering screen along our line-of-sight, while inverted arclets in the secondary spectrum can result from individually distinguishable images on the screen (Cordes et al. 2006; Walker et al. 2004). In this picture, each in-

verted arclet is due to the interference of one lensed image with the other images of the pulsar, while the main parabola is due to the interference of the bright, line-of-sight image of the pulsar with the scattered images. The discrete images have been observed to persist for weeks (Hill et al. 2003, 2005) and show minute changes in their locations with frequency (Brisken et al. 2010; Hill et al. 2005), suggesting small, long-lived substructures within the screen, which are inconsistent with the expected characteristics of isotropic turbulence in the ISM. Not only are the substructures, observed to be $\lesssim 0.1$ AU (Brisken et al. 2010; Hill et al. 2005) in size, much smaller than those expected from interstellar turbulence, but such large free electron densities, $n_e \approx 100 \text{ cm}^{-3}$ (Hill et al. 2005), are required to produce the observed scattering angles that these structures would be out of pressure equilibrium with the ISM and therefore rare, which is inconsistent with the prevalence of pulsar scintillation arcs.

Pen & Levin (2014) suggest that scintillation is instead caused by corrugated sheets, such as current sheets along which Alfvén waves with amplitudes larger than the thickness (depth) of the sheet create many crests. If the sheet is closely aligned with our line-of-sight to the pulsar and

* E-mail: simard@astro.utoronto.ca

corrugated in a perpendicular direction, a high gradient in free electron column density is achieved at each crest, resulting in large refraction angles near the crest. If many wave crests are distributed over the sheet, grazing refraction off of the sheet will result in a linear series of images, in analogy to grazing reflections off waves on a lake. (See Fig. 1 in Liu et al. (2016) for an example.) This is due to a selection effect - bending angles close to our line-of-sight can be achieved by smaller, and more common, wave crests. (Note that in contrast to surface waves on a lake, in this picture the entire depth of the sheet is perturbed by the waves, so that it resembles a flag in the wind.) If refraction is occurring due to a corrugated, closely-aligned thin sheet, the curvature of the corrugations relieves the requirement for very high electron densities within the sheet; it is the combination of the curvature and the difference in the electron density between the sheet and the ambient ISM that leads to large refraction angles. This both alleviates the tension between the prevalence of pulsar scintillation and the large overpressures of the inferred structures in the ISM and has the implication that both underdense and overdense lenses can produce the observed refraction angles; we will thus consider both cases here.

A number of lensing models have already been considered in the context of both pulsar scintillation and quasar extreme scattering events (ESEs) (Fiedler et al. 1987), lensing of quasars by the ISM. Clegg et al. (1998) model two ESEs using a Gaussian-shaped lens with a free electron overdensity. They find that the lens can produce the overall shape of the light curves observed, but that the parameters of the lens must be fine-tuned at each frequency band. Pen & King (2012) consider the effect of a Gaussian-shaped underdense lens on a point source such as a pulsar or quasar, and find that a double-peaked light curve, such as those characteristic of ESE's, is produced. Bannister et al. (2016); Tuntsov et al. (2016) model the dynamic spectrum of an ESE in an attempt to determine the electron column density and shape of the lens. They consider two lens shapes, one which is isotropic and one which is anisotropic, but find that the data holds no preference for one over the other. They find that the parameters used to model the ESE at one observing band are not suitable at another band. These results indicate that successfully modeling the lensing behaviour at a single frequency band and epoch is not enough to suggest consistency of the model with observations; a successful model must also predict changes in the scattering with time and frequency.

In this paper, we investigate the effects of a thin, corrugated plasma sheet closely aligned to our line-of-sight, like the current sheets corrugated by Alfvén waves discussed by Pen & Levin (2014), on emission from a pulsar. In Section 2 we construct a model of this lens and examine it analytically, while in Section 3 we present some numerical examples of this model. In both Sections 2 and 3 we examine the magnifications and angular separation between the images when multiple images form at a single crest and we explore the evolution of the lensing with time and frequency. Observations which can be compared to this model are discussed in Section 4 and extensions to this model are considered in Section 5. We finish with concluding remarks in Section 6.

2 THE MODEL

In the picture of scattering from a corrugated sheet presented by Pen & Levin (2014), each wave crest along the inclined sheet produces an image of the pulsar and each crest can be parameterized from properties of the wave and the observing geometry, as shown in Fig. 1. The lensing in this picture can be explored in different ways. One can consider how properties of the sheet, including the thickness of the sheet and the distribution of waves, determine the statistical properties of the scattering, such as the angular distribution of the scattered radiation, which can be compared to the observed scattering tails or Very Long Baseline Interferometry (VLBI) correlated flux densities of pulsars. In this paper we take a different approach, and focus on the case where individual scattered images of the pulsar are distinguishable, for example as inverted arclets in the secondary spectrum. In this regime, the magnification and position of each image is related to properties of the crest producing that image. Furthermore, by tracking the image locations and magnifications through frequency and time, the dependence of the scattering on both the observing frequency and the proximity of the pulsar to the crest can be compared to the model.

With this in mind, we begin our investigation by considering a single wave crest. We choose z to be the line-of-sight direction, and x and y to be in the plane of the sky, with the origin at the crest. We will consider a sheet of thickness T corrugated in the x direction, so that all refraction occurs in the x direction. We will model the crest itself as a parabola in the x - z plane. In truth, we do not know the orientation of the sheet or the corrugations in the x - z plane, but since it is the projected curvature that determines the lensing behaviour, differences in inclination can be accounted for by changing the curvature of the parabola. We will focus on a single wave crest, and write the equation for this crest as

$$x = \frac{z^2}{2R}, \quad (1)$$

where R is the radius of curvature projected along the x direction at the apex of the crest.

We will use the lensing geometry shown in Fig. 2. In this geometry, the lens equation is

$$\theta = \beta + s\hat{\alpha}, \quad (2)$$

where θ is the observed position of the source, β is the true position, $\hat{\alpha}$ is the bending angle, $s = 1 - d_{\text{lens}}/d_{\text{psr}}$, d_{psr} is the distance to the pulsar plane, and d_{lens} is the distance to the lens plane. We determine $\hat{\alpha}$ by considering Φ , the phase change imparted by the lens,

$$\Phi(x) = \frac{2\pi}{\lambda} \int dz(n(x) - n_0), \quad (3)$$

where n_0 is the index of refraction outside of the lens, n is the index of refraction inside the lens, and λ is the wavelength of observations. The bending angle is related to the gradient of the phase change by

$$\hat{\alpha}(x) = -\frac{\lambda}{2\pi} \nabla_x \Phi(x). \quad (4)$$

Assuming that the index of refraction is constant inside of the lens, this reduces to

$$\hat{\alpha}(x) = -\Delta n \nabla_x Z(x), \quad (5)$$

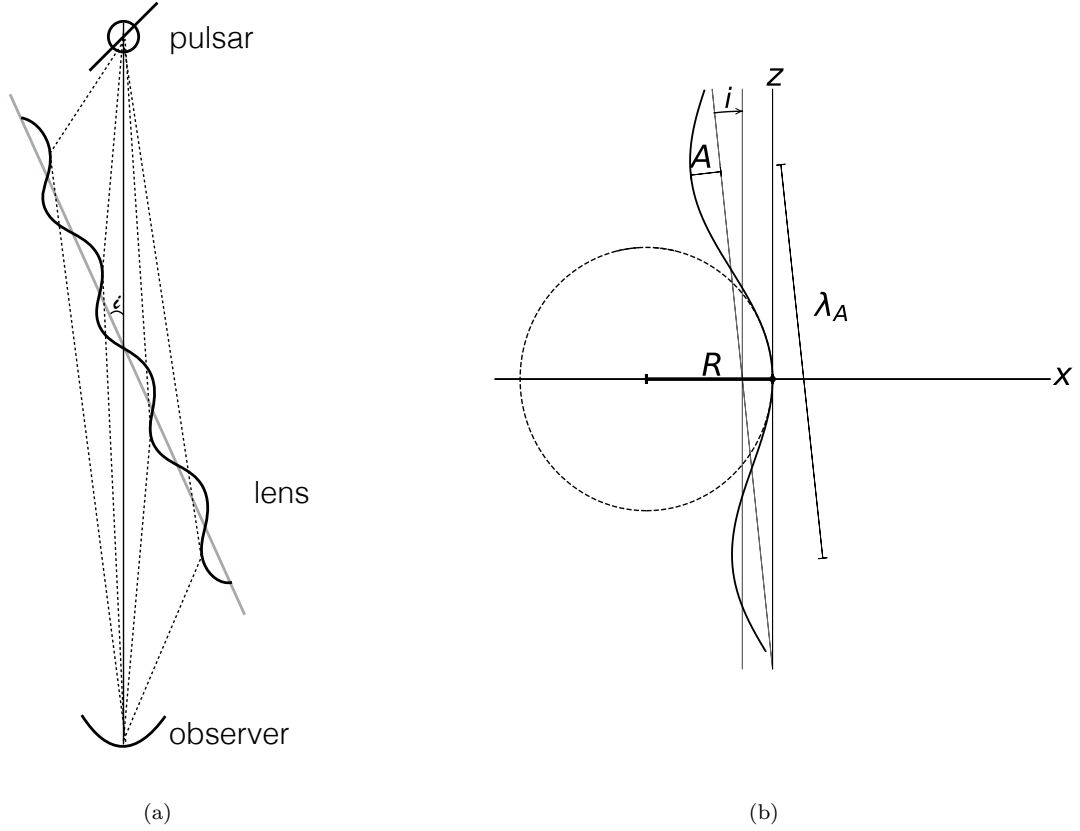


Figure 1. The geometry of lensing from an inclined sheet. Figure 1a shows how multiple wave crests result in many images of the pulsar. The line of sight image is shown with the solid line, while the dotted lines indicate the lensed images. The grey solid line shows the orientation of the sheet, and i is the inclination angle between the sheet and the line of sight to the pulsar. The specific ray deflections shown are those that would result if the corrugated sheet were underdense. Figure 1b shows the relation between the radius of curvature at the location where the column density gradient is maximized and the parameters of the wave perturbing the sheet. The thick curve represents the sheet, perturbed by a sinusoidal wave with wavelength λ_A and amplitude A , and inclined by an angle i relative to the line-of-sight to the source. The column density through the lens is maximized at the origin, and the dashed circle is the osculating circle, with radius R , at this point. Note that these figures are not to scale: We've drawn the lensing sheet to occupy the whole distance between the observer and the pulsar, while in reality it only occupies a small percentage, we expect dozens of crests along the current sheet rather than the few that we've drawn, and the angle i is much less than 1.

where $\Delta n = n - n_0$ and Z is the extent of the lens in the z -direction. In the regime $x \gg T/2$, $Z = 2T \frac{dl}{dx}$, where dl is the length element of the lens, $dl^2 = dz^2 + dx^2$. The factor of 2 comes from the two sides of the parabola. Using equation (1) for the shape of the lens, we find

$$\nabla_x Z = 2T \frac{d^2 l}{dx^2} = -\frac{TR}{2x^2 \sqrt{R/2x + 1}}, \quad (6)$$

so that we can write

$$\hat{\alpha}(x) = \Delta n \frac{TR}{2x^2 \sqrt{R/2x + 1}}. \quad (7)$$

For a plasma, the index of refraction is given by

$$n = \sqrt{1 - \frac{\omega_p^2}{\omega^2}}, \quad (8)$$

where $\omega_p = \sqrt{4\pi c^2 r_e n_e}$ is the characteristic frequency of the plasma expressed in terms of the electron density, n_e , and the classical electron radius, $r_e = \frac{1}{4\pi\epsilon_0} \frac{e^2}{m_e c^2}$ where ϵ_0 is the

vacuum permittivity and m_e is the mass of the electron. For $n_e = 0.03 \text{ cm}^{-3}$, a typical value for the ISM, this characteristic frequency is 1.5 kHz, much smaller than the GHz frequencies of typical radio observations. Therefore, we approximate the index of refraction as

$$n \simeq 1 - \frac{\lambda^2}{2\pi} n_e r_e. \quad (9)$$

We now write the bending angle in terms of the electron density,

$$\hat{\alpha}(x) = -\frac{\lambda^2}{2\pi} \Delta n_e r_e \frac{TR}{2x^2 \sqrt{R/2x + 1}}, \quad (10)$$

where Δn_e is the difference between the free electron densities inside and outside of the sheet. Since we measure angular positions on the sky, rather than physical ones, we will use the dimensionless variables $\theta = x/d_{\text{lens}}$, $r = R/d_{\text{lens}}$ and $\theta_T = T/d_{\text{lens}}$, and write:

$$\hat{\alpha}(\theta) = -\frac{\lambda^2}{2\pi} \Delta n_e r_e \frac{\theta_T r}{2\theta^2 \sqrt{r/2\theta + 1}}. \quad (11)$$

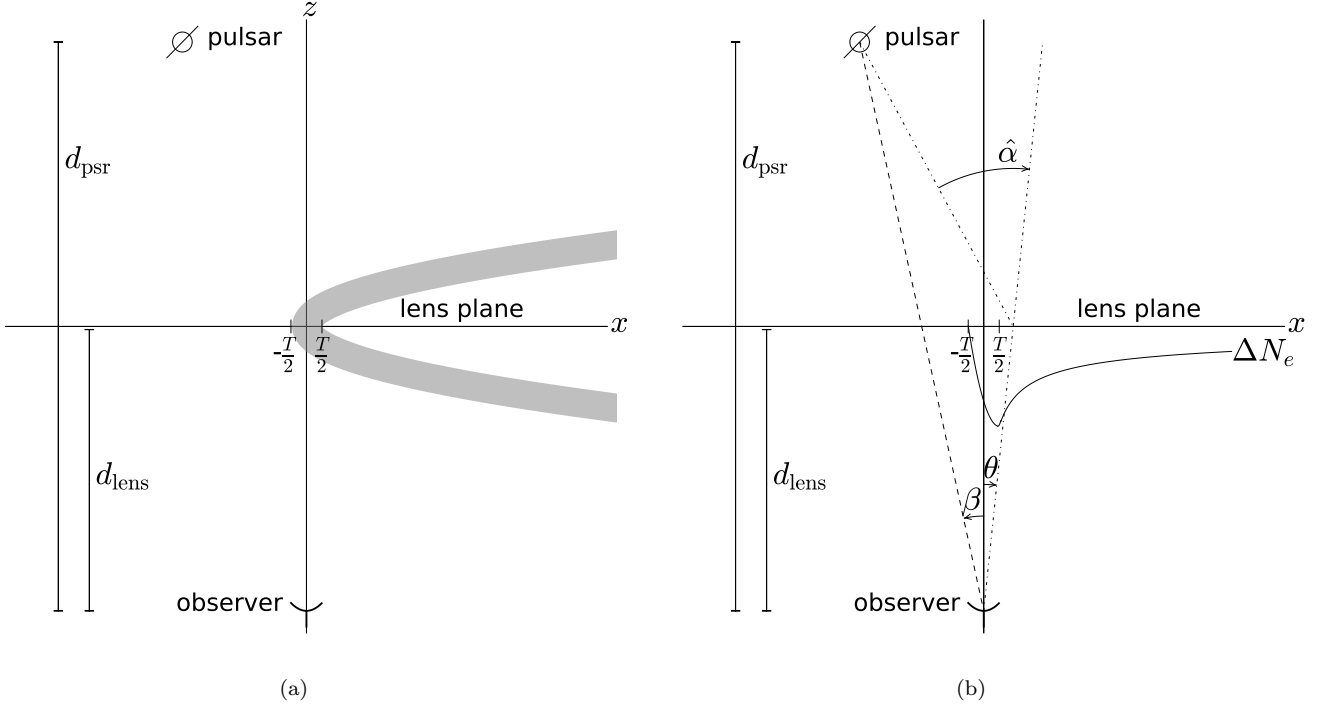


Figure 2. Lensing geometry and definitions of variables that we will use in this paper. The grey curve in Fig. 2a represents a single crest the sheet, while the solid curve in Fig. 2b is a sketch of the column density profile of the lens. The angles θ and β are measured clockwise from the line from the observer to the crest of the corrugation, so that $\beta < 0$ as drawn. The angle $\hat{\alpha}$ is measured clockwise from the line between the pulsar and the image of the pulsar on the lens plane. Note that in practice the angles are all much smaller than 1 and the crest covers only a very small portion of the line-of-sight to the pulsar. The specific deflection angle and column density profile shown are those for an underdense corrugated sheet.

We now write the lens equation for this system,

$$\theta = \beta - s \frac{\lambda^2}{2\pi} \Delta n_e r_e \frac{\theta_T r}{2\theta^2} \frac{1}{\sqrt{r/2\theta + 1}}. \quad (12)$$

We see that increasing the over or underdensity, radius of curvature, or thickness of the lens results in a larger deflection.

Under the approximation that $\theta \ll r/2$, equation (12) simplifies to

$$\theta \simeq \beta - s \frac{r_e \lambda^2}{2\sqrt{2}\pi} \frac{\Delta n_e \theta_T \sqrt{r}}{\theta^{3/2}} \quad (13)$$

$$\simeq \beta + \frac{s}{\sqrt{2}} \frac{\Delta n \theta_T \sqrt{r}}{\theta^{3/2}}, \quad (14)$$

where we have used equation (9) to write the lens equation in terms of Δn . We see that under this approximation the lens equation depends only on the frequency of observation, the distances to the pulsar and lens, and a single physical parameter describing the lens itself, $\Delta n \theta_T \sqrt{r}$; in other words, the column density and radius of curvature of the lens are degenerate. Throughout this paper, we will use this approximation to analyze the behaviour of the lens; however all numerical results are calculated using the full form of the lens equation, equation (12).

The solution to the lens equation gives the observed angular positions, θ , of the pulsar for a given true angular position, β . Due to conservation of surface brightness, the

magnification of the lensed image is

$$\mu = \left(\frac{d\beta}{d\theta} \right)^{-1}. \quad (15)$$

Using equation (13), this evaluates to

$$\mu \simeq \left(1 + \frac{3s}{2\sqrt{2}} \frac{\Delta n \theta_T \sqrt{r}}{\theta^{5/2}} \right)^{-1}. \quad (16)$$

We will now consider two possibilities - either the sheet is underdense or it is overdense. We will approximate the sheet as a thin sheet to simplify the following analytic analysis. Within this approximation, we will consider the lens to be at $\theta > 0$, with no lens at $\theta < 0$. If the sheet is overdense, then the index of refraction in the sheet is less than that in the ambient ISM ($\Delta n < 0$), and the bending angles produced are negative (see equation (11)). If instead the sheet is underdense, $\Delta n > 0$ and the bending angles produced are positive.

We can understand the general behaviour of the lens by considering the function $\beta(\theta)$:

$$\beta = \theta - \frac{s \Delta n \theta_T \sqrt{r/2}}{\theta^{3/2}}. \quad (17)$$

When θ is large, $\beta \approx \theta$, while when θ is small, $\beta \propto \theta^{-3/2}$ if the lens is overdense and $\beta \propto -\theta^{-3/2}$ if the lens is underdense. There is a lensed image at $\beta = 0$ when

$$\theta_0 \equiv \left(s \Delta n \theta_T \sqrt{r/2} \right)^{2/5}, \quad (18)$$

which has a single real solution if the sheet is underdense but no solutions if the sheet is overdense. Finally, we see that local extrema occur when $\frac{d\beta}{d\theta} = 0$, or

$$\theta_{\text{ext}} \equiv \left(-\frac{3}{2}s \Delta n \theta_T \sqrt{r/2} \right)^{2/5}. \quad (19)$$

If the lens is underdense, there are therefore no local extrema, but if the lens is overdense there is one, a local minimum.

Combining this information, we see that if the lens is underdense there is a single lensed image for all β , or all true positions of the pulsar. In addition, the unlensed image of the pulsar is visible if $\beta < 0$. As a result, two images are visible if $\beta < 0$, the unlensed image and a lensed image. If $\beta > 0$, only one, lensed image is seen, but it tends towards the line-of-sight position for large β . If the lens is overdense, then there are two lensed images for $\beta > \beta(\theta_{\text{ext}}) > 0$, one at small θ and one at $\theta \approx \beta$. There is only the line-of-sight image at $\beta < 0$, and there are no images at all for $0 < \beta < \beta(\theta_{\text{ext}})$.

From equation (16), differences in the brightnesses of the lensed images between the two lenses are apparent. If the lens is underdense, $\Delta n > 0$, and $\mu < 1$, so that lensed images brighter than the unlensed image of the pulsar cannot be produced. When $\beta = 0$ and $\theta = \theta_0$, we find that the magnification of the image is $\frac{2}{5}$, regardless of the lens parameters. If the lens is overdense, $\Delta n < 0$, so that $\mu > 1$ or $\mu < 0$. In this case, either the lensed image is brighter than the unlensed image of the pulsar, or the image is inverted.

In practice, as discussed later in Section 4, we do not measure the absolute magnifications and locations of the lensed images, but rather the magnification ratio and angular displacement between two images of the pulsar. To compare with observations, we will therefore investigate the magnification ratios and angular separations between images in the cases where two images are formed at a single crest.

We can derive a relation between the magnification ratio and angular separation by assuming that the brightest image is unlensed, which for the underdense lens is true, and for the overdense lens is a good approximation when $\beta \gg (s|\Delta n| \theta_T \sqrt{r/2})^{2/3}$. We will write the location and magnification of the brightest image as $\theta_0 \approx \beta$ and $\mu_0 \approx 1$ respectively. In this case, the angular separation is

$$\begin{aligned} \Delta\theta &\approx \theta - \beta \approx \frac{s}{\sqrt{2}} \frac{\Delta n \theta_T \sqrt{r}}{\theta^{3/2}} \\ &\approx 3.6 \text{mas} \frac{s}{1/2} \frac{\Delta n}{1.3 \times 10^{-11}} \frac{\theta_T}{4 \times 10^{-10}} \sqrt{\frac{r}{10}} \left(\frac{\theta}{1 \text{mas}} \right)^{-3/2}, \end{aligned} \quad (20)$$

where θ is the angular location of the fainter image. (See Section 3.1 for the origin of the fiducial values chosen for Δn , θ_T , r and θ . For most pulsar scintillation systems, the screen is not associated with the pulsar and is midway between the observer and the pulsar, so we choose a fiducial value $s = 1/2$.) This allows us to write θ in terms of the angular separation, $\Delta\theta$:

$$\theta \approx \left(\frac{s}{\sqrt{2}} \frac{\Delta n \theta_T \sqrt{r}}{\Delta\theta} \right)^{2/3}. \quad (22)$$

In this regime, we expect the magnifications of the faint images to be much less than one. We can therefore simplify

equation (16):

$$\mu \approx \frac{2\sqrt{2}}{3} \frac{1}{s} \frac{\theta^{5/2}}{\Delta n \theta_T \sqrt{r}}. \quad (23)$$

We now combine equations (22) and (23) to write the magnification ratio in terms of the angular separation:

$$\begin{aligned} \left| \frac{\mu}{\mu_0} \right| &\approx \frac{2}{3} \left(\frac{s}{\sqrt{2}} \frac{|\Delta n| \theta_T \sqrt{r}}{\Delta\theta} \right)^{2/3} |\Delta\theta|^{-5/3} \\ &\approx 0.03 \left(\frac{s}{1/2} \frac{|\Delta n|}{1.3 \times 10^{-11}} \frac{\theta_T}{4 \times 10^{-10}} \sqrt{\frac{r}{10}} \right)^{2/3} \left| \frac{\Delta\theta}{10 \text{mas}} \right|^{-5/3}. \end{aligned} \quad (24)$$

Equation (24) can be rewritten as

$$\left| \frac{\mu}{\mu_0} \right| \approx \frac{2}{3} \left| \frac{\Delta\theta_{\text{ref}}}{\Delta\theta} \right|^{5/3}, \quad (26)$$

where

$$\Delta\theta_{\text{ref}} = \left(\frac{s}{\sqrt{2}} \frac{|\Delta n| \theta_T \sqrt{r}}{\Delta\theta} \right)^{2/5} \quad (27)$$

$$\approx 1.7 \text{mas} \left(\frac{s}{1/2} \frac{|\Delta n|}{1.3 \times 10^{-11}} \frac{\theta_T}{4 \times 10^{-10}} \sqrt{\frac{r}{10}} \right)^{2/5}. \quad (28)$$

Therefore, we expect $\left| \frac{\mu}{\mu_0} \right| \propto |\Delta\theta|^{-5/3}$ for large separations. This relation allows us to determine $\Delta\theta_{\text{ref}}$, and therefore $|\Delta n| \theta_T \sqrt{r}$, from observations of the angular separations and relative magnifications of the images from a single wave crest. Note that if the sheet is underdense, $\Delta\theta_{\text{ref}}$ is the angular separation when the pulsar is directly behind the crest, $\Delta\theta(\beta = 0) = \theta_0$. (See equation (18).)

We can also consider the frequency evolution of the lensing qualitatively. The bending angle $\hat{\alpha} \propto -\frac{\Delta n}{\theta^{3/2}}$ when $\theta \ll r/2$ and the index of refraction scales with wavelength, $\Delta n \propto \lambda^2$, so that at higher frequencies, images near the crest of the wave must form at smaller θ . In the underdense case, the line-of-sight image of the pulsar is at $\beta < 0$ when a second lensed image is visible, so that as the lensed image moves towards the crest of the wave the angular separation between the line-of-sight and lensed images decreases. In contrast, if the lens is overdense two images are visible when $\beta > 0$, the bright image of the pulsar at approximately the line-of-sight to the pulsar and a faint image close to the crest of the wave. In this case, as the wavelength increases the fainter image moves to smaller θ while the brighter image moves very little with wavelength, so that the angular separation between the two images increases. Thus, we see that if the lens is underdense, the angular separation between the two images decreases with frequency, while if it is overdense the angular separation increases with frequency. This behaviour allows one to distinguish between the two cases, and determine the sign of the lensing parameter $\Delta n \theta_T \sqrt{r}$.

3 NUMERICAL EXAMPLES

In order to construct some numerical examples of this model, we first put some values to parameters in the model in Section 3.1. We then consider the behaviour of a single wave crest for lenses of varying strengths in Section 3.2. Finally,

we present an example of constraining the lens parameter and predicting the evolution of the lensed images with time and frequency in Section 3.3.

3.1 Numerical Parameters

For our numerical model, we will adopt parameters from one of the most thoroughly studied examples of pulsar scintillation arcs, PSR B0834+06. We will assume the distances to the pulsar and lens are those measured by Liu et al. (2016) for PSR B0834+06 and one of its lensing screens, $d_{\text{psr}} = 620$ pc, $d_{\text{lens}} = 389$ pc. We will assume an observing frequency of 314.5 MHz. For a typical lensed image, we will consider an angular displacement from the line-of-sight image of the pulsar of 10 mas and a magnification of 0.01, parameters similar to those measured by Brisken et al. (2010) for PSR B0834+06. Finally, in order to predict the temporal evolution of this system, we will need to know the speed with which the pulsar moves behind the lens in the direction of scattering. For this, we will also use the value measured by Liu et al. (2016), 172.4 km s^{-1} , or an angular relative velocity of 1.12 mas/week .

We will assume values for T , the thickness of the sheet, and R , the radius of curvature of the crest, and vary only the electron density, and thus the index of refraction, inside the lens, but keep in mind that this model only constrains the combination of parameters $\Delta n \theta_T \sqrt{r}$ and not Δn itself. In physical parameters, for a sheet with an inclination angle i relative to the line-of-sight to the pulsar, the radius of curvature at the point where the tangent is in the z -direction is

$$R = \frac{\lambda_A^2}{4\pi^2 A \cos^3(i)} \frac{1}{\sqrt{1 - \frac{\lambda_A^2}{4\pi^2 A^2} \tan^2(i)}} \quad (29)$$

$$\approx \frac{\lambda_A^2}{4\pi^2 A}, \quad (30)$$

where λ_A and A are respectively the wavelength and amplitude of the Alfvén wave. See Figure 1b for a sketch of the wave and the resulting radius of curvature. In order to corrugate the current sheet, the amplitude of the wave must be much greater than the thickness of the sheet, and we expect a very small inclination angle of the sheet with respect to our line-of-sight, $i \ll 1$, in order to produce the linear series of images observed. We expect the projected wavelength, $\lambda_A \sin(i)$, to be similar to the separation between images, which in some cases is as small as 0.05 AU for the PSR B0834+06 system (Brisken et al. 2010).

We choose an Alfvén wavelength $\lambda_A = 10^5$ AU, an inclination of the sheet with respect to our line-of-sight to the pulsar $i = 10^{-5}$ rad, a thickness of the sheet $T = 0.03$ AU or $\theta_T = 0.08$ mas, and an amplitude of the Alfvén wave $A = 0.3$ AU. These parameters give a projected wavelength of 1 AU, and a projected radius of curvature at the apex of the parabola of $R = 4.8$ kpc or $r = 12$. Assuming a volume filling factor of 10% (Draine 2011) for the warm ionized interstellar medium, and an average electron density throughout the entire ISM of 0.03 cm^{-3} , we assume a typical electron density of 0.3 cm^{-3} in the warm ionized interstellar medium. While our analysis does not depend on this value, it does inform the physically allowed electron density differences between

the lens and the surrounding medium: We will consider electron density differences between inside and outside the lens of $\Delta n_e = \pm 0.3, \pm 0.003 \text{ cm}^{-3}$.

3.2 Lensing from a single crest

Using equations (12) and (15), we can calculate the angular positions and magnifications of images for lenses of varying strengths, shown in Fig. 3. When examining these figures, recall that the part of the lens we are considering is at $\theta \geq \theta_T/2$, with maximum strength at $\theta = \theta_T/2$. From Fig. 3, we can confirm that multiple images are produced by the underdense lens when the pulsar is not behind the crest, and multiple images are produced by the overdense lens when the pulsar is behind the crest. We also note that magnifications larger than 1 occur only in the overdense case. If the lens is overdense, the fainter image is inverted, as indicated by the negative magnification, and there is a range in β for which we see no images at all as the line-of-sight to the pulsar is obscured by the lens and the lens is bending light out of our sight.

The numerical relation between the angular separation and flux ratio of two images formed at a single wave crest is shown in Fig. 4. We see that after each curve is scaled by the reference separation, $\Delta\theta_{\text{ref}}$ (equation (27)), the relation between magnification ratio and angular separation is independent of the lens parameters. By measuring the angular separation and flux ratio for a pair of images, we can determine the value of $\Delta\theta_{\text{ref}}$ required to place the point along the curves in Fig. 4, and therefore $|\Delta n| r \sqrt{\theta_T}$, provided that the distance to the pulsar is known.

3.3 Time and frequency evolution of the system

Once the free parameter of the lens, $|\Delta n| \theta_T \sqrt{r}$, is constrained from the magnification ratios and angular separations, changes in the locations and magnifications of the images with frequency can be predicted. If the angular velocity of the pulsar relative to the screen in the x -direction (parallel to the axis along which the images are formed; see Fig. 2), $\frac{(V_{\text{psr}} - V_{\text{lens}})_{\parallel}}{d_{\text{psr}}}$, is also known, we can predict changes over time. Since we do not know if the lens is overdense or underdense at this stage, we consider both cases.

As an example, we will consider two images with a magnification ratio of 0.01 and an angular separation of 10 mas at a frequency of 314.5 MHz. Using these values, we calculate that the lens has, for the parameters given in Section 3.1, $|\Delta n_e| = 0.007 \text{ cm}^{-3}$. From the lens equation and the angular separation, we now determine the true position of the pulsar relative to the crest, β , for the underdense and overdense cases, -9.9 and 10.2 mas respectively. Let's assume that the angular separation is decreasing as the pulsar moves towards the crest. In the case of the overdense lens, after 4 weeks, the magnification ratio of the 2 images has increased to 0.028, and the angular separation has decreased by 4.6 mas. The magnification ratio of the images will continue to increase and the images will continue to get brighter until the two images have zero angular separation after 7.6 weeks, after which the lensed image will disappear. In the case of the underdense lens, after 4 weeks, the angular separation

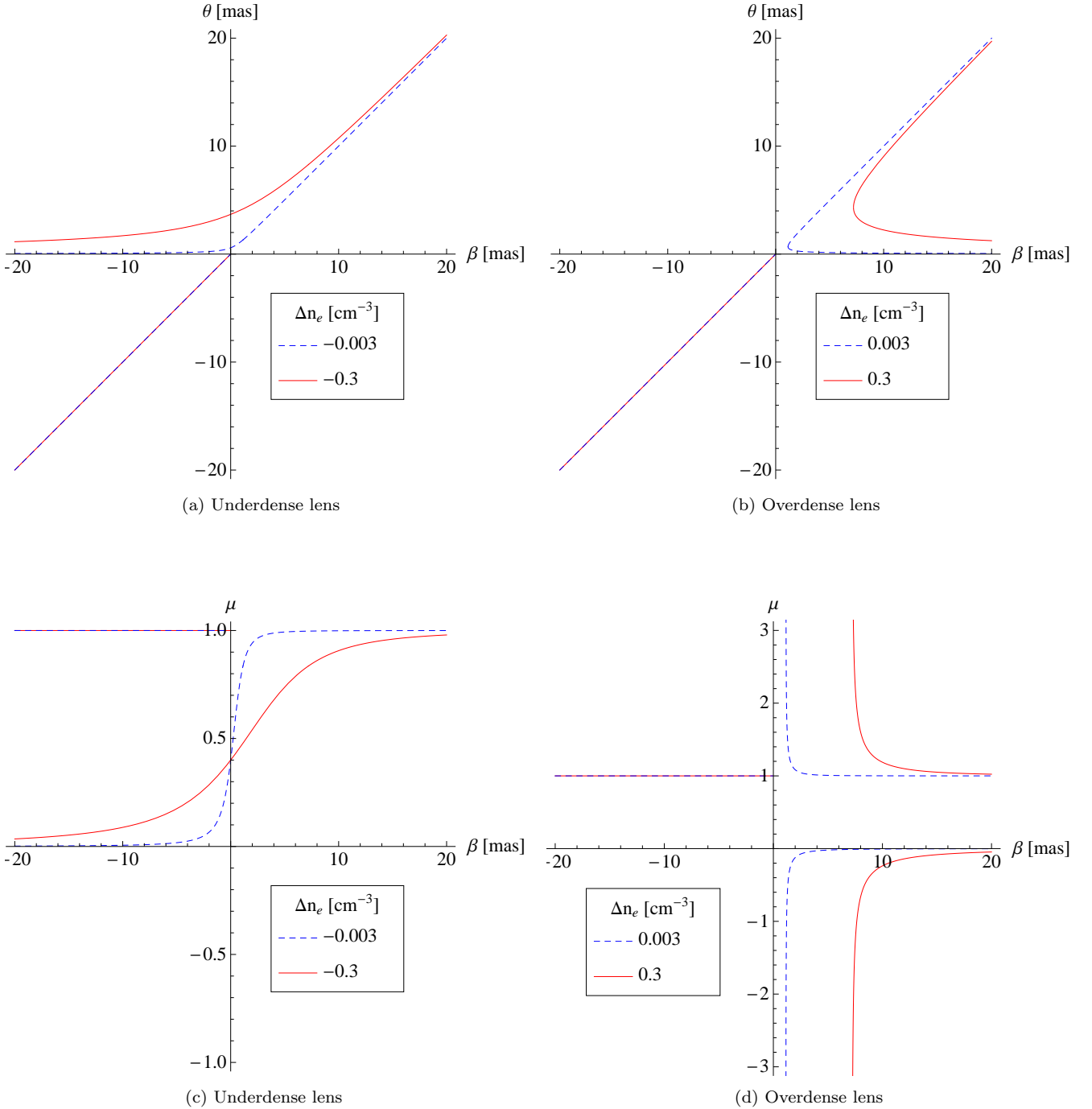


Figure 3. The observed position of the pulsar, θ , and magnification, μ , as a function of the true position, β . The legend indicates the difference between the free electron density inside and outside of the lens, Δn_e when the parameters in Section 3.1 are assumed. Recall that the lens we are considering is at $\theta > \theta_T/2$, or $\theta > 0.04$ mas. In the underdense lens case, a lensed image is observed along with the true, unlensed image of the pulsar before the pulsar passes behind the crest, as the lens is bending light from the pulsar into our line-of-sight. The angular separation between these two images reaches a minimum, non-zero value just as the pulsar passes behind the crest ($\beta = 0$), and the magnification of the lensed image at this point is $\frac{2}{5}$, independent of the lens parameters. After the pulsar passes behind the crest, the line-of-sight image to the pulsar is obscured by the lens, and a single, lensed image is observed. In the case of an overdense lens, only the line-of-sight image is seen before the pulsar is passing behind the crest as the lens bends light out of our line-of-sight. Just after the pulsar has passed behind the lens, no images are seen, as the line-of-sight image is obscured by the lens, and the lens is still bending light out of our line-of-sight. There is a minimum β for which two images are produced, and at which the two images have zero angular separation and are both strongly magnified. The angular separation between the images grows as the pulsar moves to larger β . The unlensed image is at $\theta = \beta$ and $\mu = 1$ for all lenses when $\beta < -\theta_T/2$.

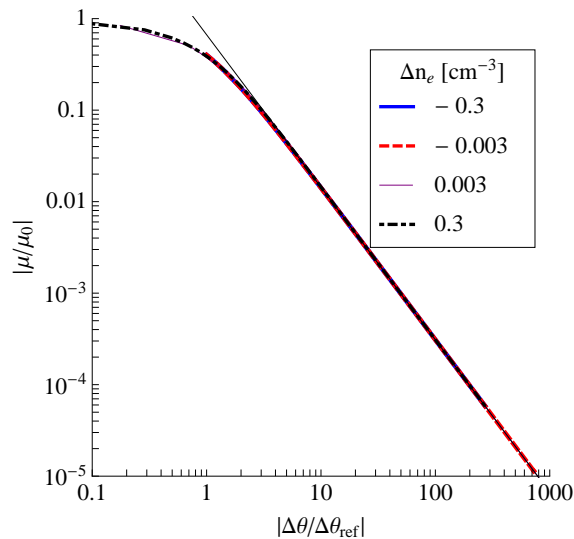


Figure 4. The ratio of the magnification of the fainter image, μ , to the magnification of the brighter image, μ_0 , as a function of the angular separation, $\Delta\theta$, between two images formed at a single wave crest, scaled by the reference value, $\Delta\theta_{\text{ref}}$ (equation (27)). The legend indicates the difference between the electron density inside and outside the lens, Δn_e when the parameters in Section 3.1 are assumed. The reference separations are 0.58 and 3.68 mas for Δn_e of ± 0.003 and $\pm 0.3 \text{ cm}^{-3}$ respectively, and the solid black line shows the analytical relation at large separations, equation (26). After these shifts in angular separation, the curves for various values of the lens parameter lie directly on top of one another, although the curves for an overdense sheet extend to smaller angular separations due to the minimum angular separation in the underdense case. This allows one to measure the parameter describing the lens, $\Delta n_e \theta_T \sqrt{r}$, up to the sign of Δn_e , from measurements of $|\mu/\mu_0|$ and $\Delta\theta$ by determining the reference separation required to align the point with the curves. Further observations, such as the change in angular separation with wavelength, can then be used to determine whether the lens is overdense or underdense.

between the two images has decreased by 4.4 mas, and the magnification of the lensed image is 0.026.

Similarly, we can consider changes with frequency. Using the same example, we examine how the angular separation between the two images varies over a 32-MHz frequency band from 310.5 MHz to 342.5 MHz and find that, for the underdense lens, the angular separation will decrease by 0.019 mas moving from the lowest to highest frequencies in the band, while the magnification ratio decreases by 0.0012. For the overdense lens, the angular separation increases by 0.022 mas from the lowest to highest frequencies in the band, while $|\mu/\mu_0|$ decreases by 0.0013. We fit a power law to the relation between angular separation and wavelength over this band for both the underdense and overdense lenses. The best fit power law exponents are shown in Table 1. In the underdense case, the power law exponent is positive, meaning that at higher frequencies the images are closer together, while in the overdense case it is negative, so that at higher frequencies the images are further apart. This is also apparent from Figs. 3a and 3b: Since $\Delta n \propto -\Delta n_e \lambda^2$, observing at longer wavelengths has the same effect as increasing the strength of the lens, and one can see from Figs. 3a and 3b that when the lens is stronger (or at lower frequencies) the angular separation is larger if the corrugated sheet is underdense, but smaller if the corrugated sheet is overdense. Briskin et al. (2010) statistically combine arclets in the secondary spectrum of PSR B0834+06 and measure positive

Table 1. Power law fits of the form $\Delta\theta = B\lambda^\gamma$ to the change in separation with wavelength for a lens that produces two images with an angular separation of 10 mas and a flux ratio of 0.01 at 314.5 MHz. The fit is done over 310.5 MHz to 342.5 MHz. While the exponents here are small, exponents of the same order of magnitude have been measured over the same bandwidth with 10 to 20% uncertainties by Briskin et al. (2010).

$\Delta n_e \text{ [cm}^{-3}\text{]}$	γ
-0.0067	0.019
0.0067	-0.023

power law exponents, 0.062 ± 0.006 and 0.019 ± 0.004 , over this 32-MHz band for two of three identified arclet groups (for the third group, they find that the separation does not vary with wavelength within the measurement uncertainties), suggesting that the sheet is underdense and indicating that the small exponents predicted by this model are measurable.

4 MEASUREMENTS OF PULSAR SCATTERING

The main phenomenon this model hopes to reproduce is the existence of parabolic arcs in the secondary spectra of pulsars, which can arise from highly anisotropic scattering at a

thin sheet along our line-of-sight to the pulsar. Using global VLBI to obtain the secondary cross-spectrum between two stations, the angular locations of the images relative to the line-of-sight image of the pulsar can be measured (Briskin et al. 2010). Under the thin sheet approximation, the distance and velocity of the sheet can be determined from the relationship between the measured angular separations of two images and the Doppler frequency and delay of the feature in the secondary spectrum resulting from the interference between these images. If inverted arclets, evidence of distinguishable images on the screen, are present in the secondary spectrum, the location of these in the secondary spectrum combined with the distance and velocity of the sheet can be then used to obtain the positions of the images to $\approx 1\%$ accuracy (Briskin et al. 2010), a technique known as ‘back-mapping’. Using additional techniques, such as holography, the precision of these measurements can be improved even further (Pen et al. 2014). The relative fluxes of inverted arclets in the secondary spectrum encodes the relative fluxes of the images of the pulsar on the scattering screen, providing us with the rest of the information required to constrain the model. To test temporal evolution of the scattering against this model, we also need to know the whether the angular separation between an image and the line-of-sight image to the pulsar is increasing or decreasing. If the Doppler frequency of the arclet corresponding to an image is negative, then the pulsar is moving towards the image and the angular separation is decreasing. If the Doppler frequency is positive, then the pulsar is moving away from the image, and the angular separation is increasing.

This model may also be applied to pulse echoes, such as those observed in the Crab pulsar (eg. Backer et al. 2000; Lyne et al. 2001), PSR B2217+47 (Michilli et al. 2018) and at least one other pulsar (Oslowski *et al.*, in prep.). In these cases, radio interferometry can be used to measure the angular position of the echo relative to the main pulse, while the pulse profile itself can be used to determine the magnification of the echo. Combining the angular information with the delay of the echo relative to the main pulse allows one to determine the geometry and velocities (if one has multi-epoch observations of the system) of the scattering system. By correlating the unlensed pulse with the echo, the phase imparted by the lens can be retrieved. If the image is inverted, the waveform of the image will be distorted (Dai & Venumadhav 2017), allowing a direct test for the inversion of the image in this case. Some pulsars have giant pulses, short, intense bursts of radiation, that exhibit scattering tails from interstellar scattering. Giant pulses allow the response of the lens to be determined from the scattering of a single pulse (Main et al. 2017), making these systems even more promising for detecting image inversion.

5 EXTENSIONS

5.1 The region of the lens $-\theta_T/2 < \theta < \theta_T/2$

So far, we have considered only the portion of the crest where $\theta > \theta_T/2$. However, we expect additional images from the region $-\theta_T/2 < \theta < \theta_T/2$. The maximum extent of the lens along the line-of-sight occurs at $\theta = \theta_T/2$, so that the gradient $\nabla_x Z$ has opposite sign for $|\theta| < \theta_T/2$ and $\theta > \theta_T/2$, and

therefore the bending angle, which is proportional to this gradient, switches direction at $\theta = \theta_T/2$.

We can treat the region $-\theta_T/2 < \theta < \theta_T/2$ as a separate lens, and we can parameterize the lens as being bounded by the line

$$z = \sqrt{(R+T)(x+T/2)}. \quad (31)$$

The thickness of the lens is then

$$Z = 2\sqrt{(R+T)(x+T/2)}, \quad (32)$$

and, once again assuming the index of refraction is constant within the lens, the bending angle induced by the lens is

$$\hat{\alpha}(x) = -\Delta n \nabla_x Z \quad (33)$$

$$= -\Delta n \sqrt{\frac{R+T}{x+T/2}} \quad (34)$$

$$\hat{\alpha}(\theta) = -\Delta n \sqrt{\frac{r+\theta_T}{\theta+\theta_T/2}}, \quad (35)$$

so that the lens equation for this system is:

$$\theta = \beta - s\Delta n \sqrt{\frac{r+\theta_T}{\theta+\theta_T/2}}. \quad (36)$$

From equation (36), we see that the region $-\theta_T/2 < \theta < \theta_T/2$ corresponds to $\beta \geq \frac{\theta_T}{2} + s|\Delta n| \sqrt{\frac{r+\theta_T}{\theta_T}}$ if the lens is underdense,

and to $\beta \leq \frac{\theta_T}{2} - s|\Delta n| \sqrt{\frac{r+\theta_T}{\theta_T}}$ if the lens is overdense.

Once again, we can determine the magnification of the image produced from the derivative of the lens equation:

$$\mu = \left(\frac{d\beta}{d\theta}\right)^{-1} \quad (37)$$

$$= \left(1 - \frac{s\Delta n \sqrt{(r+\theta_T)/4}}{(\theta+\theta_T/2)^{3/2}}\right)^{-1}. \quad (38)$$

We see that if $\theta_T \gtrsim (s|\Delta n| \sqrt{(r+\theta_T)/4})^{2/3}$, a very highly magnified image can occur in the region $-\theta_T/2 < \theta < \theta_T/2$ and would need to be considered. However, if $\theta_T \ll (s|\Delta n| \sqrt{(r+\theta_T)/4})^{2/3}$, which holds for the parameters in Section 3.1, the magnification is instead maximized when $\theta = \theta_T/2$, and reaches a value

$$|\mu|_{\max} \approx \frac{\theta_T^{3/2}}{s|\Delta n| \sqrt{(r+\theta_T)/4}}. \quad (39)$$

For the parameters in Section 3.1 and $\Delta n_e = 0.3 \text{ cm}^{-3}$, $|\mu|_{\max} = 9 \times 10^{-5}$, much fainter than the images produced at $\theta > \theta_T/2$. We see from equation (39) that if $\theta_T \ll (s|\Delta n| \sqrt{(r+\theta_T)/4})^{2/3}$, the images produced by the region $-\theta_T/2 < \theta < \theta_T/2$ are very faint compared to the unlensed image.

The constraints on the angular positions of the pulsar at which this faint image appears result in a minimum angular separation between the faint image and the bright image, or line-of-sight image, of the pulsar,

$$|\Delta\theta|_{\min} \approx \theta_T/2 - \beta(\theta_T/2) \quad (40)$$

$$= s|\Delta n| \sqrt{\frac{r+\theta_T}{\theta_T/2}}. \quad (41)$$

This is exact when the sheet is overdense, and the faint image from $-\theta_T/2 < \theta < \theta_T/2$ appears simultaneously with the line-of-sight image to the pulsar. If the sheet is underdense, the faint image appears simultaneously with the lensed image at positive β , but as this faint image from $-\theta_T/2 < \theta < \theta_T/2$ appears only at large β , where the bright lensed image from $\theta > \theta_T/2$ appears at $\theta \approx \beta$, this approximation is very good. For the parameters in Section 3.1 and $\Delta n_e = 0.3 \text{ cm}^{-3}$, $|\Delta\theta|_{\text{max}} \approx 2000 \text{ mas}$. In contrast, in the secondary spectrum of PSR B0834+06, scattered flux appears up to an angular separation of 28 mas. Since this is less than the minimum angular separation between the line-of-sight image of the pulsar and the faint image from $-\theta_T/2 < \theta < \theta_T/2$, we see once again that we can ignore the images from this region of the lens. At larger thicknesses, the lensed images become brighter and move to lower angular separations, where they can complicate the analysis and should be considered.

Due to the change in lensing direction at $\theta = \theta_T/2$, we may be able to place independent constraints on the thickness of the sheet. Consider the case where a faint image from a region $\theta > \theta_T/2$ is moving towards smaller θ as the pulsar moves away from the crest. Once the image reaches $\theta = \theta_T/2$, if the pulsar continues to move further from the crest, the lens will no longer be able to bend the pulsar light into our line-of-sight, and the faint image and corresponding echo or arclet in the secondary spectrum will disappear. This sets a maximum angular separation between the two images when $\theta_{\text{maxsep}} = \theta_T/2$. If this maximum angular separation could be observed, then from the angular separation and magnifications of the images we could determine the parameter of the lens, the true position, β , and the lensed position, $\theta_{\text{min}} = \theta_T/2$ from $\Delta\theta_{\text{ref}}$ (e.g. Section 3.2). If we know the distance to the lens, we can also calculate the physical thickness of the lens, T . For the parameters in Section 3 and $\Delta n_e = 0.3 \text{ cm}^{-3}$, the maximum angular separation is 3000 mas, at which the flux ratio between the two images is -8×10^{-6} . Typical secondary spectra analyses are not sensitive to angular separations larger than approximately 30 mas, so the maximum angular separation is not expected to be observable as a sudden disappearance of the lensed image.

5.2 A smooth lens profile

In previous sections, we have considered the effects of a lens profile with a discontinuous derivative. This is due to our assumption that the density within the sheet is constant, so that the density does not vary smoothly across the sheet. We can relax this assumption with a more general treatment, with which we can consider any density profile through the sheet, $\Delta n_{e,\text{sheet}}(d)$, where d is the depth through the unbent sheet, normal to the plane of the sheet.

We write the bending angle, α as:

$$\alpha = -s \frac{\lambda^2}{2\pi} r_e \nabla_x \Delta N_e(x), \quad (42)$$

where $\Delta N_e(x) = \int_{-\infty}^{\infty} dz (n_e(x, z) - n_{e,0})$ and $n_{e,0}$ is the free electron density in the ambient ISM. We can approximate $N_e(x)$ as the convolution of the profile of the corrugated sheet and

the electron density profile through the sheet, $\Delta n_{e,\text{sheet}}(d)$:

$$\Delta N_e(x) = \int_{-\infty}^{\infty} dX \Delta n_{e,\text{sheet}}(X) 2 \frac{dl}{dx} \Big|_{x-X}. \quad (43)$$

This is a good approximation when the tangent to the corrugated sheet is near parallel with our line of sight to the pulsar, such as near the crest of a wave on the sheet. In order to compare between different density profiles, we normalize the electron density profile through the sheet so that

$$\int_{-\infty}^{\infty} dd \Delta n_{e,\text{sheet}}(d) = T \Delta n_e, \quad (44)$$

where $T = 0.03 \text{ AU}$ and $\Delta n_e = 0.3 \text{ cm}^{-3}$.

We consider a Gaussian form of the electron density profile,

$$\Delta n_{e,\text{sheet}}(d) = \frac{\Delta n_e T}{\sqrt{2\pi} s} \exp\left(-\frac{d^2}{2s^2}\right), \quad (45)$$

where $s = \frac{T}{2\sqrt{2 \ln(2)}}$ and $\Delta n_{e,\text{sheet}}(d)$ has a FWHM of T , as an example of a smoothly-varying density profile and contrast this with a top-hat electron density profile,

$$\Delta n_{e,\text{sheet}}(d) = \Delta n_e \Theta(T/2 - d) \Theta(T/2 + d), \quad (46)$$

where Θ is the Heaviside step function. This top-hat electron density profile, allows us to extend the model discussed in previous sections of this paper, where we investigated a top-hat electron density profile using analytic approximations, to the entire lens, including those regions where our previous approximations did not hold.

The lens profiles are shown in Fig. 5, and the solutions to the lens equation, $\theta(\beta)$ and $\mu(\beta)$, are shown in Fig. 6, where we see that the behaviour at $|\theta| \gg \theta_T$ (0.08 mas for these examples) does not depend on the specifics of the density profile through the lens. However, when $|\theta| \lesssim \theta_T$, the bending angles in the case of the top-hat sheet profile diverge. This is in contrast to the Gaussian sheet, which adheres to the odd-image theorem and produces additional images compared to the top-hat sheet. These images are normally very faint but are highly magnified when $\frac{d\beta}{d\theta} = 0$. These highly-magnified events occur for large bending angles, when the pulsar is far from the crest of the wave, and for only a small range in β , and thus in time. Typical secondary spectrum analyses are sensitive to $|\Delta\theta| \lesssim 30 \text{ mas}$, and therefore do not need to account for these highly magnified images. In addition, due to the chromatic nature of the lensing, these events occur at a specific β for only a small range in frequency, and thus are expected to be much less apparent when observing with a wide bandwidth.

We can also look at how the number of images produced by the lensing system varies with both the observing frequency and the offset between the pulsar and the crest of the wave, shown in Fig. 7. When observing these images, keep in mind that during the transition between regions of one and three images events of high magnification occur. As expected from our discussion in previous sections, we see that additional high-magnification events occur in the overdense case compared to the underdense case.

5.3 Many images from a single sheet

In practice, we often observe many lensed images of a pulsar. In the picture presented in this work, each of these images

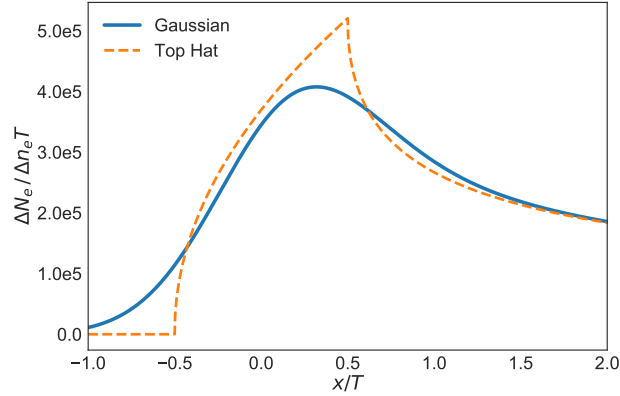


Figure 5. The lens profiles as a function of x for a top hat (orange dashed line) and a Gaussian (blue solid line) electron density profile through the sheet. Note that the lens profile is continuously differentiable for the Gaussian electron density profile, but that the lens profile from a top hat electron density profile, like that considered analytically in the sections above, has a discontinuous derivative at $x = -T/2$ and $x = T/2$. As a result, the corrugated Gaussian sheet adheres to the odd-image theorem while the corrugated top hat sheet does not.

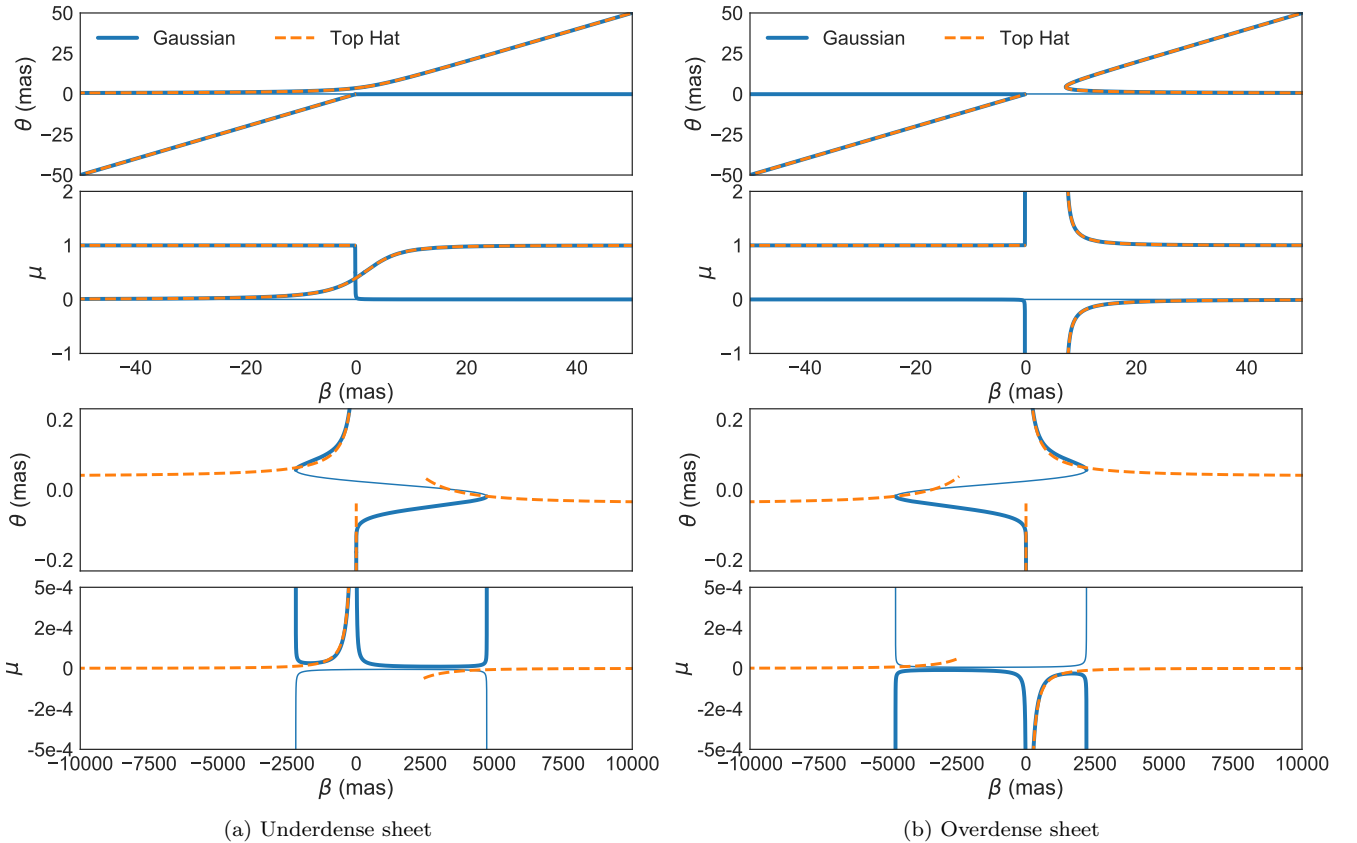


Figure 6. The solution to the lens equation for the lens profiles in Fig. 5. From the top two panels of each subfigure, we see that when $\theta \gg \theta_T$, the lens behaviour does not depend on the electron density profile through the sheet apart from the extra image formed near $\theta = 0$ when the sheet has a Gaussian profile. In the bottom two panels, we have adjusted the axis to focus on region $|\theta| < \theta_T$ and highlight the differences that arise between the two electron density profiles. We have drawn the extra image produced when a smooth Gaussian density profile through the sheet is considered with a thin line to distinguish it from the other images.

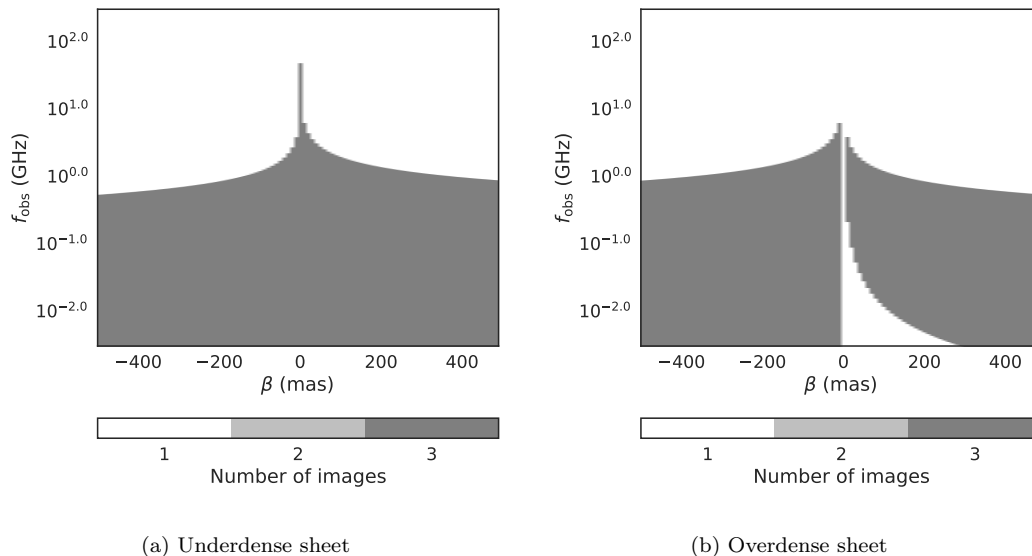


Figure 7. The dependence of the number of images produced on observing wavelength, λ_{obs} , and the location of the pulsar relative to the crest of the wave, β , for a sheet with a Gaussian electron density profile. Both an underdense (Fig. 7a) and overdense (Fig. 7b) sheet are considered. We see that this model adheres to the odd-image theorem, as there are only regions of 1 or 3 images.

is from a different wave crest on the sheet. Each wave crest may have a different value of $\Delta n \theta_T \sqrt{r}$, and so the analysis above can be done for every wave crest, or equivalently every inverted arclet in the secondary spectrum or every echo of the pulsar.

While in some pulsars the individual images are distinguishable in the secondary spectrum as individual inverted arclets, in many cases these inverted arclets are not resolved, adding ambiguity to modeling the lensing in terms of individual wave crests. Holographic techniques (*e.g.* Pen et al. 2014; Walker et al. 2008) can retrieve the electric field due to the combination of images, which may assist in identifying individual images, and we can additionally consider statistical phenomena that arise when we have lensing from multiple crests, such as the scattering tail of a single pulse, the spread of pulse power over time due to the delays imparted by the various crests. This requires numerical simulations that take into account the distribution of waves along the sheet, and is deferred to future work.

5.4 Symmetric lensing events

Although we have focused on pulsar scintillation, the picture discussed within this paper can also lead to symmetric lensing events. Consider two consecutive crests which extend from the plane of the sheet in opposite directions. If the crests are very close together, as shown in Fig. 8, then a very high column density through the lens is achieved at $x = 0$, and the column density profile is symmetric in x . Further quantitative analysis, outside of the scope of this paper, is necessary to confirm the qualitative similarities between this set-up and the observed characteristics of symmetric lensing events such as ESEs. In particular, the ability of this model to predict both the light curves and frequency evolution of these events must be studied. While these events are expected to be generic, as with any corrugated sheet there

is an inclination angle for which the line of sight to the pulsar is parallel to the tangent through the sheet at $x = 0$, an approximation of the prevalence of this event requires assumptions of both the distribution of plasma sheets in the ISM and the distribution of wavelengths and amplitudes of waves along those sheets, and is thus beyond the scope of the paper. However, this feature of the corrugated sheet model presented here may also explain why both symmetric and asymmetric features are seen in the echoes of the Crab pulsar (Lyne et al. 2001).

6 CONCLUSIONS

We have investigated the effects of a corrugated plasma sheet as the source of pulsar scintillation arcs. Using geometric optics, we calculate the number of images and magnifications of these images as a pulsar moves behind a wave crest on one of these sheets. We find that in the limit $\theta \ll r/2$ the lens can be described by a single parameter, $\Delta n \theta_T \sqrt{r}$, which can be constrained from observations of the pulsar. Once this parameter is known, this model can be used to predict how the magnifications and locations of the images will change over time and frequency, providing a concrete test of this model. In particular, we see that over a small band of 32 MHz we expect changes in the locations of the images comparable to those measured by Briskin et al. (2010). We also see that we expect very different behaviour from an overdense sheet or an underdense sheet: In the overdense case, the angular separation between two images increases at higher frequencies, while in the underdense case it decreases at higher frequencies. Briskin et al. (2010) find that the separation decreases with frequency for two of three identified groups of images in the secondary spectrum of PSR B0834+06, suggesting that the lens is underdense. There are other qualitative differences between the underdense and overdense lenses: magnifications greater than 1 occur only when the sheet is over-

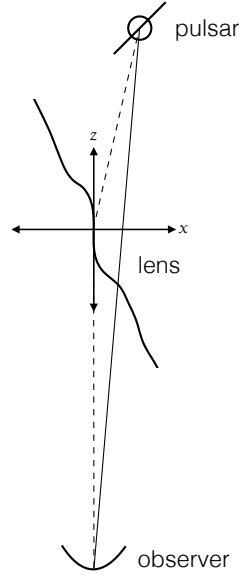


Figure 8. A geometry of the corrugated sheet which can produce symmetric events. Due to the orientation of the sheet combined with the locations of the two crests, the lens has a symmetric column density profile that results in large bending angles at $x = 0$. Note in the picture we are considering, the sheet only occupies a small percentage of the distance between the source and the observer, and the angle between the sheet and the line-of-sight to the pulsar is much less than one.

dense, both images of the pulsar disappear when the pulsar is just behind the crest of the wave in the overdense case, and only the overdense lens produces inverted images.

Qualitatively, there are two major differences between this model and previous models of ESEs and pulsar scintillation arcs. Other authors (*e.g.* Bannister et al. 2016; Clegg et al. 1998; Pen & King 2012; Tuntsov et al. 2016) have considered smoothly varying electron column densities, which adhere to the odd image theorem and produce one or three images. In this work, we see that when we consider an abrupt change in density at the sheet boundary, the column density considered is not continuously differentiable, and the lens produces one or two images. When we consider a smooth density profile within the sheet, our lens does adhere to the odd-image theorem. However, due to the thinness of the sheet considered, the additional images formed are faint at angular separations of interest to pulsar scintillation studies, and can be safely ignored. In addition, we have considered an asymmetric lens that may explain asymmetric dispersion and scattering events, such as the anomalous dispersion measure variations seen in PSR J1713+0747 (Jones et al. 2017; Lentati et al. 2016) and asymmetric echo events observed in the Crab pulsar (Lyne et al. 2001).

In future work, we will apply this test to observations of pulsar scintillation and of pulsar echoes. The simplest test comes from observations of pulsars with well-defined inverted arclets in their secondary spectra, as these arclets can be mapped to images on the sky through VLBI observations (Brisken et al. 2010) and therefore to individual wave crests in the current sheet. Ideal observations will be at low frequencies where scintillation effects are strongest and over a wide bandwidth in order to measure the changes in the secondary spectrum over frequency. We can also compare this model to observed changes in the secondary spectrum over time. For this, we desire many observations of the pulsar on

week to month long timescales. Finally, we can simulate and test features of this model that arise when we consider many images of a single pulsar being created by multiple crests, such as the scattering tail of a highly scattered pulsar. The results of these tests will assess the consistency of the corrugated, closely aligned, sheet model with observations of pulsar scintillation.

ACKNOWLEDGEMENTS

We thank Marten van Kerkwijk and Robert Main for many valuable discussions from the early stages of this work. We also thank Dan Stinebring and Barney Rickett for useful suggestions, and Peter Martin for helpful discussions. We thank the referee for comments that have much improved the paper. DS acknowledges funding from NSERC. The Dunlap Institute for Astronomy and Astrophysics is funded through an endowment established by the David Dunlap family and the University of Toronto.

References

- Backer D. C., Wong T., Valanju J., 2000, *ApJ*, 543, 740
- Bannister K. W., Stevens J., Tuntsov A. V., Walker M. A., Johnston S., Reynolds C., Bignall H., 2016, *Science*, 351, 354
- Brisken W. F., Macquart J.-P., Gao J. J., Rickett B. J., Coles W. A., Deller A. T., Tingay S. J., West C. J., 2010, *AJ*, 708, 232
- Clegg A. W., Fey A. L., Lazio T. J. W., 1998, *ApJ*, 496, 253
- Cordes J. M., Rickett B. J., Stinebring D. R., Coles W. A., 2006, *ApJ*, 637, 346
- Dai L., Venumadhav T., 2017, preprint (arXiv:1702.04724)
- Draine B. T., 2011, *Physics of the Interstellar and Intergalactic Medium*

- Fiedler R. L., Dennison B., Johnston K. J., Hewish A., 1987, *Nature*, 326, 675
- Hill A. S., Stinebring D. R., Barnor H. A., Berwick D. E., Webber A. B., 2003, *ApJ*, 599, 457
- Hill A. S., Stinebring D. R., Asplund C. T., Berwick D. E., Everett W. B., Hinkel N. R., 2005, *ApJ*, 619, L171
- Jones M. L., et al., 2017, *ApJ*, 841, 125
- Lentati L., et al., 2016, *MNRAS*, 458, 2161
- Liu S., Pen U.-L., Macquart J.-P., Briskeen W., Deller A., 2016, *MNRAS*, 458, 1289
- Lyne A. G., Pritchard R. S., Graham-Smith F., 2001, *MNRAS*, 321, 67
- Main R., van Kerkwijk M., Pen U.-L., Mahajan N., Vanderlinde K., 2017, *ApJ*, 840, L15
- Michilli D., et al., 2018, *MNRAS*
- Pen U.-L., King L., 2012, *MNRAS*, 421, L132
- Pen U.-L., Levin Y., 2014, *MNRAS*, 442, 3338
- Pen U.-L., Macquart J.-P., Deller A. T., Briskeen W., 2014, *MNRAS*, 440, L36
- Putney M. L., Minter A. H., Stinebring D. R., Ransom S. M., 2005, in *Bull. American Astron. Soc.* p. 1470
- Stinebring D., 2007, in Haverkorn M., Goss W. M., eds, Vol. 365, *SINS - Small Ionized and Neutral Structures in the Diffuse Interstellar Medium ASP Conference Series*. p. 254
- Stinebring D. R., McLaughlin M. A., Cordes J. M., Becker K. M., Goodman J. E. E., Kramer M. A., Sheckard J. L., Smith C. T., 2001, *ApJ*, 549, L97
- Tuntsov A. V., Walker M. A., Koopmans L. V. E., Bannister K. W., Stevens J., Johnston S., Reynolds C., Bignall H. E., 2016, *ApJ*, 817, 176
- Walker M., Melrose D., Stinebring D., Zhang C., 2004, *MNRAS*, 354, 43
- Walker M. A., Koopmans L. V. E., Stinebring D. R., van Straten W., 2008, *MNRAS*, 388, 1214

This paper has been typeset from a $\text{\TeX}/\text{\LaTeX}$ file prepared by the author.